Quasi-static and high strain rate response of aluminum matrix syntactic foams under compression

Kyle MYERS[a], Bálint KATONA[b], Pedro CORTES[a,c], Imre Norbert ORBULOV[b,d,]*

[a] Materials Science and Engineering, Youngstown State University, Youngstown, OH 44555, USA

[b] Department of Materials Science and Engineering, Faculty of Mechanical Engineering, Budapest University of Technology and Economics, Bertalan Lajos utca 7., Budapest, Hungary, 1111

[c] Civil / Environmental and Chemical Engineering, Youngstown State University, Youngstown, OH 44555, USA

[d] MTA–BME Research Group for Composite Science and Technology, Műegyetem rakpart 3., Budapest, Hungary, 1111

*Corresponding author

Address: Department of Materials Science and Engineering, Faculty of Mechanical Engineering, Budapest University of Technology and Economics, Bertalan Lajos utca 7., Budapest, Hungary, 1111

Tel: +36 1 463 2386

Fax: +36 1 463 1366

E-mail: orbulov@eik.bme.hu, orbulov@gmail.com

Abstract

Aluminum alloy matrix syntactic foams were produced by inert gas pressure infiltration. Four different alloys and ceramic hollow spheres were applied as matrix and filler material, respectively. The effects of the chemical composition of the matrix and the different heat-treatments are reported at different strain-rates and in compressive loadings. The higher strain rates were ~~ensured~~ performed in~~by~~ a Split-Hopkinson pressure bar system. The results show that, the characteristic properties of the materials strongly depends on the chemical composition of the matrix and its heat-treatment condition. The compressive strength of the investigated foams showed a limited sensitivity to the strain rate, its effect was more pronounced in the case of the structural stiffness and fracture strain. The failure modes of the foams have explicit differences showing barreling and shearing in the case of quasi-static and high strain rate compression respectively.

Keywords: A. Foams; B. Fracture; B. Mechanical properties; C. Mechanical testing

1. Introduction

Metal matrix syntactic foams (MMSFs) are particle reinforced composites, filled by hollow spheres. This type of material is interesting since when compared to other metal foams it combines lower maximum porosity and higher density with greatly increased quasi-static compressive strength. Moreover, it maintains the advantages and useful properties of metal foams such as low density, thermal and environmental resistance. In most cases the matrix material is aluminum alloy, but steel [1-5], magnesium [6] and titanium [7-9] matrices have also been investigated. As reinforcement, commercially available ceramic [10-15] or metallic [10] hollow spheres are the most common systems on MMSFs. Additional serious efforts have been made to reduce the cost of MMSFs by using low cost perlite [16-18] or pumice [19].

MMSFs can be applied in numerous fields;~~.~~ f~~F~~or ~~example~~instance, due to their damping capacity and low density features, ~~~~they can be used as ~~make them applicable materials for~~as automotive brake rotors, and steer rods, ~~~~etc.~~ or as ~~for different~~ covers / hulls / packaging (sandwich cores) structures. T~~Indeed, t~~heir ~~high energy~~high-energy absorption capabili~~ty~~ty~~city~~

2

and high compressive strength can also be beneficial in crash energy absorption zones (aerospace and ground transportation) and protective panels' applications (vehicles, buildings). MMSFs also have shown electromagnetic (EM) damping properties that can be applied in the EM and microwave shielding field.

The main loading mode of metallic foams is compression, and the compressive behavior of MMSFs has been widely studied [20-27]. Due to its importance, their testing methodology and characteristic properties under quasi-static conditions have been summarized in standard procedures [28]. However, the effects of higher strain rates have not completely investigated. This would be important in the perspective of collision dampers or protective applications. For example, Balch et al. fabricated aluminum matrix / hollow ceramic microsphere syntactic foams (SFs) by liquid metal infiltration of commercially pure and 7075 aluminum. The SFs showed quasi-static compressive strengths of 100 MPa and 230 MPa, respectively. The dynamic compression tests proved ~10–30% increase in peak strength compared to the quasi-static results, and the strain rate sensitivities of these foams were similar to those of aluminum matrix composite materials [29]. Luong et al. determined the strain rate dependence of compressive response for A4032 aluminum alloy/hollow fly ash cenosphere composites. They reported that the composite showed a higher strength and a energy absorption capability at higher strain rates [30]. Similar tests were performed on AZ91D magnesium alloy composites filled with 5 wt% hollow fly ash cenospheres. Compared to the matrix alloy, the energy absorption was higher in their counterpart composites at comparable strain rates [31]. Luong et al. also studied the quasi-static and dynamic properties of aluminum alloy matrix SiC hollow particle reinforced (A356/SiC) SFs. The composites were manufactured using SiC hollow spheres with identical outer diameter (~1 mm), but with different wall thicknesses (67.8±13.6 and 79.3±20.5 μm). The different types of SFs had a specific quasi-static compressive strength of 89.1 and 87.4 MPa/(gcm^{-3}), and a specific high strain rate (2100 s^{-1}) compressive strength of 81.2 and 76.1 MPa/(gcm^{-3}), respectively. It was determined that the samples did not show strain rate sensitivity [23, 32]. Gupta et al. produced Mg based SFs with extremely low density (0.97 gcm^{-3}), filled with SiC

3

hollow spheres. The peak strength and the elastic energy absorbed up to the peak strength showed <u>an</u> increasing trend <u>by</u>~~with~~ increas<u>ing the</u>~~ed~~ strain rates (<u>from</u> 1330 <u>to</u> ~~–~~2300 s⁻¹). The values at high strain rate were up to 1.5 times higher than the corresponding quasi-static values. The failure at high strain rates was observed to be crushing of the particles, plastic deformation of the matrix, and propagation of cracks along the precipitates on the grain boundaries [33]. Santa-Maria et al. determined the quasi-static and dynamic mechanical properties of A380–Al₂O₃ MMSFs with six different microsphere sizes and different size ranges. The tests were conducted at strain rates between 880 and 1720 s⁻¹ and revealed that the properties of MMSFs containing hollow spheres with an average diameter of 0.425–0.85 and 0.85–1 mm were not strain rate-dependent and, therefore, their performance would have been similar to that determined from quasi-static tests [24]. Zou et al. investigated the dynamic mechanical behavior of aluminum matrix SFs <u>using a</u>~~by~~ Split-Hopkinson pressure bar system. The MMSFs were fabricated by pressure infiltration technique and had a porosity ratio of 45%. The energy absorption capability of the SFs exceeded 70% under dynamic loading <u>than that shown under</u>~~versus under~~ quasi-static loading rates. During the deformation process, the syntactic foam exhibited a ~~well~~ <u>remarked</u> energy absorption capability due to the reduction of original pores in SFs ~~accused~~ <u>caused</u> by cenospheres rupture. Hence, ~~the~~ aluminum matrix SFs are ~~considerably~~ <u>suitable for</u> ~~suit~~ applications <u></u>~~for the varied protective devices~~ <u>in the</u> aerospace and automobile ~~applications,~~ <u>field</u> due to their high strength–density ratio and excellent energy absorption capabilities [34]. Dou et al. investigated the high strain rate compression behavior of cenosphere–pure aluminum SFs, and compare their performance to that displayed under quasi-static loading rate conditions. <u>It was found that t</u>~~T~~he foams exhibited distinct strain rate sensitivity and <u>that</u> the peak strengths increased from ~45–75 to ~65–120 MPa. Also, they observed an increase in the energy absorption capacity by ~50–70% [35]. Goel et al. studied the compression behavior of aluminum cenosphere SFs at strain rates ranging from quasi-static conditions to 1400 s⁻¹. The compressive strength and energy absorption of the investigated foams attained a maximum at strain rates of approximately 750 s⁻¹<u>,</u> and then decreased as the strain rate increased. <u>It was also found that t</u>~~T~~he foam with coarser cenosphere<u>s</u> appeared to be more ~~sensitive to~~ strain rate <u>sensitive</u>. An empirical relation was also developed to predict

4

the dynamic compressive strength of the aluminum cenosphere based SFs [36-38]. Fiedler et al. addressed the dynamic analysis of low cost expanded perlite/aluminum (EP/A356) SFs under dynamic compressive loading conditions. Stresses were found to slightly increase at higher strain rates, indicating positive strain-rate sensitivity. The perlite particles had positive effect on the compression resistance at high loading velocities. A possible explanation was connected to the pressure built-up of the entrapped air within the particles, and the stabilization of adjacent metal struts [39]. Mondal et al. assessed the deformation response and energy absorption characteristics of closed cell aluminum-fly ash particle composite foams under compressive loading conditions at different strain rates (from 10^{-2} to 10^{1} s^{-1}). The influence of strain rate on the deformation responses was found to be very marginal; the strain rate sensitivity was measured to be very low (0.02–0.04) when the foam relative density was greater than 0.1, while it was found to be negative when the foam relative density was less than 0.1 [40, 41]. Lehmhus, Peroni et al. studied the mechanical behavior of syntactic foams made of glass microspheres mixed in an iron matrix. Different types of foams were investigated varying the strength of the glass and its weight percentage content. The experimental characterization was performed by means of compression tests at three different strain-rate levels. The results showed that the strain-rate behavior of the foams was mainly governed by the matrix. ItThis was justified (based on the experimental results), that after the plateau in the densification region, the curves seem to remain parallel to each other [42-44]. Rabiei et al. produced steel–steel and aluminum–steel composite metal foams (CMFs) with different sphere sizes by standard powder metallurgy and gravity fed casting techniques. When comparing the specific energy absorption of the CMFs at 50% strain of the same loading rates, the smaller 2.2 mm sphere CMF absorbed about 30% more energy than the larger 5.2 mm sphere CMF at high loading rates. As the loading rate increased, a consistent improvement of the yield strength of the material was also observed [45-47].

All these previous works, reveal useful information about the dynamic compressive properties of specific grade foams. However, the effect of the chemical composition of the metallic matrix and of heat-treatment were not reported. Therefore the aim of the present paper is to extend the

5

available data ~~about~~ regarding the quasi-static and dynamic compressive properties of MMSFs ~~with~~ based on different matrices and different heat-treatment conditions.

2. Materials and experimental methods

2.1. Investigated materials and production

The investigated MMSFs were produced by the combination of commercially available aluminum alloys (Al99.5, AlSi12, AlMgSi1 and AlCu5) and Globocer grade ceramic hollow spheres provided by Hollomet GmbH [10]. The nearest ASM equivalent, the nominal chemical compositions, the ultimate tensile strength (UTS) values (in solution treated state, for comparison) and the melting point ($T_{melting}$) of the applied aluminum alloy matrix materials are listed in Table 1. The composition was measured by an EDAX Genesis energy dispersive X-ray spectroscope (EDS) and only the significant elements are tabulated. The reinforcement, consisting of ceramic hollow spheres were made of the combination of Al_2O_3 (33 wt%), amorphous SiO_2 (48 wt%) and mullite ($3Al_2O_3 \cdot 2SiO_2$, 19 wt%) as measured by XRD and EDS. The true (particle) density of the hollow spheres was 0.816 gcm^{-3}, and their average diameter and wall thickness was Ø1444±79.9 µm and 58.0±3.21 µm respectively. Here, the volume fraction of the hollow spheres on each manufactured MMSF was maintained at ~~65~~ 64 vol%; typical for randomly close packed structure [48, 49].

The investigated MMSFs were produced by liquid state, inert gas assisted pressure infiltration technique. In this process the molten matrix alloy was squeezed in between the ceramic hollow spheres. Here, a~~A~~ carbon steel mold was coated with a thin carbon layer, and filled up to half height with ~~the~~ hollow spheres. The carbon layer ensured the easy removal~~ing~~ of the ~~produced~~manufactured MMSF block after the ~~i~~infiltration process~~ing~~. An (Al_2O_3) insulator layer was placed on top of the spheres; ~~t.~~ The role of this layer was to separate the matrix materials from the spheres during the first part of the infiltrating procedure. Finally, an aluminum block (which acted as the matrix material) was placed into the container. ~~and two thermocouples (for temperature control), were placed into the container.~~ Subsequently~~Then~~, the ~~prepared and filled~~ mold ~~.~~was placed~~put~~ into the pressure infiltration chamber, and ~~. In the chamber, vacuum or gas pressure can be generated.~~ Argon (Ar) gas was used to provide the required threshold

6

pressure for infiltrating. During the first part of the infiltration procedure, heating and a rough vacuum were applied, and once The melted matrix metal formed a liquid cork above the reinforcement, the pressure was increased to a set value. The generated pressure difference above and under the liquid metal cork induced the metal to infiltrate into the reinforcement across the insulator layer. The casting temperature and pressure of the MMSF blocks was set to $T_{melting}$ + 50°C and 400 kPa respectively, while the infiltration time (during which the infiltration pressure was maintained) was set to 10 s. During the manufacturing process, the infiltration parameters were continuously monitored by a computer controlled data acquisition system. After the injection of the molten matrix, the mold was cooled, and the MMSF block removed for machining. For further details about the production phase, please refer to [50, 51].

After the production, the density and the porosity of the produced blocks were investigated. The theoretical density (ρ_T) was calculated from the density of the constituents (ρ_S and ρ_M for the hollow spheres and for the matrix, respectively) and from the volume fraction (V_S) of the hollow spheres (Eq. 1).

$$\rho_T = V_S \rho_S + (1 - V_S)\rho_M \qquad\qquad \text{eq. 1.}$$

On the other hand, the real densities (ρ_R) of each block were measured by the Archimedes' method, and the porosity in the samples, introduced by the hollow spheres (P_S) was calculated by Eq. 2.

$$P_S = V_S \left(\frac{r}{R}\right)^3 \qquad\qquad \text{eq. 2.}$$

where r and R are the inner and outer radii of the hollow spheres, respectively. Additional porosity may also exist in the matrix of the blocks, due to the possibility of insufficient infiltration pressure. This, unintended porosity (P_U) was determined by Eq. 3.

$$P_U = (1 - V_S)\frac{\rho_T - \rho_R}{\rho_T} \qquad\qquad \text{eq. 3.}$$

Due to the nature of liquid pressure infiltration (64 vol%, homogeneous distribution of hollow spheres, isotropic properties) the density can be considered homogeneous and valid for all specimens. All these calculated and measured values are listed in Table 2. Here, the negative values shown in the unintended porosity indicate

that that means a part of the hollow spheres wasere infiltrated and consequently, the therefore decreased the total porosity (P_T) decreased.

All of the specimens were homogenized ('-O' tag at the end of the specimens' designation) at 520°C for 30 min. The specimens were cooled in water, and the compression tests were performed immediately after the homogenization process, to avoid any cold aging effect (especially in the case of the AlCu5 matrix). The AlMgSi1 and AlCu5 specimens were also tested in an aged condition ('-T6' tag in the designation), involving a 14 hours long aging process at 170°C (followed by water cooling) just after the homogenization stage. Again, the T6 treated specimens were investigated immediately after the aging process.

2.2. Experimental

Cylindrical specimens with the dimensions of Ø12.7 mm for the quasi-static and the high strain rate compression tests were machined from the produced MMSF blocks. The aspect ratio of the specimens was H/D=1 in all cases, and the specimens were heat-treated, following the aforementioned homogenization or T6 treated process.

The quasi-static compression tests were performed on a MTS 810 type universal testing machine in a four column tool at room temperature. The surfaces of the tool were grinded and polished. The specimens and the tool were lubricated with anti-seize material. The average strain rate was 0.01 s^{-1}, which ensured quasi-static compression. Six specimens were compressed from each specimen group, up to 50% engineering strain to get representative results and to verify repeatability (overall, 36 specimens were tested). The tests were performed and evaluated according to the ruling standard of compression tests on cellular materials [28]. The high strain rate compression testing was conducted using a split-Hopkinson pressure bar (SHPB). Both the incident and transmission bars were made of a C-350 maraging steel with a Young's modulus of 195 GPa. The length and diameter of the bars were 1.8 m and Ø19.05 mm respectively. Strain gauges were placed at an equal distance away from the sample on both the incident and transmission bar to collect the pulse signals. The generated pulse signals were initially acquired through a signal conditioning amplifier and collected by a PicoScope oscilloscope. A 76.2 mm long striker bar was projected at the incident bar using a pressure

8

chamber filled to either 138 or 552 kPa. These incident striking pressures resulted in averaged strains rate of 933 s^{-1} and 2629 s^{-1} respectively. The stresses, strains, and strain rates were all calculated by a proprietary REL's SurePulse software. The maximum stress value was taken from the highest recorded stress value of the stress-strain curve for each sample, and the compression modulus was determined by the slope of the first 1000 data points recorded. Seven specimens were compressed from each specimen group to attainget representative results and to verify repeatability (overall, 42 specimens were tested).

To investigate the failure mechanisms, cross-section of the tested specimens were examined. The compressed specimens were cut into two halves along their axis, mounted into a resin, and grinded on an automatic grinding and polishing machine with SiC papers and diamond suspension, respectively [52-54].

3. Results and Discussion

3.1. Mechanical properties

During the compressive tests, the loading force and the deformation were registered from which the engineering stress-engineering strain curves for the quasi-static and for the high strain rate loading were calculated and plotted. Fig. 1 shows the typical engineering stress- engineering strain curves for quasi-static and for high strain rate cases (Al99.5-O;, note the similar stress, but different strain scales on the corresponding axes). In the case of compressive loading of cellular materials, the characteristic properties are particularly defined in well-known standards [28]. The initial slope of the registered curves corresponds to the structural stiffness (S (MPa)). The two main strength properties are the yield strength at 0.2% plastic strain (σ_Y (MPa)) and the compressive strength (σ_C (MPa)). In the case of Globocer reinforced MMSFs atnd quasi-static conditions, these strength values are relatively close to each other, while in the case of higher strain rates, the difference is larger. The fracture strain (ε_C (%)) is defined as the abscissa of the first local peak (compressive strength) in the engineering stress- engineering strain curve. Another important properties are the fracture energy (W_C (Jcm^{-3})) and the overall absorbable mechanical energy (W (Jcm^{-3})) during the loading process (W (Jcm^{-3})) that could be calculated

9

as the area below the registered curve up to the fracture strain, and to the end of the test, respectively.

The compressive strength values of the investigated MMSFs are plotted in Fig. 2 as the function of the matrix material, the heat treatment, and the strain rate. The figure shows that the compressive strength of the unalloyed and homogenized MMSF (Al99.5-O) ~~is~~ was lower than ~~that recorded by the~~in the case of MMSF~~s~~ with alloyed matrix ~~based alloys~~. Hence, ~~;~~. ~~This suggests that~~ the compressive strength of MMSFs ~~of the MMSFs,~~ can be effectively increased by alloying the matrix material. This phenomenon was consisten~~t~~~~d~~ on the three investigated strain rates ~~here investigated~~. The figure also shows the effect of Mg-Si (~2 wt%) and Cu (~4.5 wt%) alloying ~~-~~which resulted in a more pronounced compressive strength increment than ~~their counterpart~~pure Si alloying. ~~Here, it seems that a~~A relatively small amount of Mg-Si or Cu~~them alloying~~ was sufficient to reach the same increment as it was ensured by the ~13 wt% Si. In the quasi-static conditions, the T6 treatment of the material was also effective and ~~ensured~~ resulted in a ~40% and ~20% increment in the case of Mg-Si and Cu alloying, respectively. At higher strain rates, the increment became smaller (~10%) in the case of Mg-Si, and larger (up to ~40%) in the case of Cu alloying. Compared to the Al99.5-O MMSFs, the compressive strength was significantly increased by the strain rate;~~,~~ the average increment was ~20% and ~45% in the case of 933 s^{-1} and 2629 s^{-1} strain rates, respectively. The sensitivity to the strain rate can be quantified by the strain rate sensitivity parameter (Σ) that is defined by eq. ~~4~~4 [24, 29, 55].

$$\Sigma = \frac{\sigma_d - \sigma_q}{\sigma^*} \frac{1}{ln\left(\frac{\dot{\varepsilon}_d}{\dot{\varepsilon}_q}\right)}$$
eq. ~~1~~4.

where σ is the stress at a given strain, σ^* is the quasi-static stress, when the strain is 0.2% (σ_Y), and $\dot{\varepsilon}$ is the strain rate. The subscripts 'd' and 'q' stands for the dynamic and quasi-static loading, respectively. MMSFs can exhibit abrupt variations in stress during compression that are not seen in alloys or composites with monotonic behavior in the~~at~~ low to moderate strains regions. Therefore the compressive strength was used in the calculations of Σ, even though these peak stresses occurred at slightly different strains. The applied values, and the calculated Σ parameters are summarized in Table ~~2~~3 and plotted in Fig. 3. The strain sensitivity parameters were very low;~~,~~ the largest strain rate sensitivity parameter (0.0752) was calculated in the case of technically pure Al alloy in the homogenized state at 2629 s^{-1}. According to the

10

chemical composition of the matrix material, defined trends cannot be observed in the strain rate sensitivity parameters. However, the results based on the higher strain rate values resulted in~~gave~~ systematically higher sensitivity parameters.

The yield strength values of the investigated systems ~~investigated~~ are plotted in Fig. 4. ~~Based on the yield strength results, t~~The composition of the matrix ha~~d~~s the same effects as in the case of the compressive strength. However, the strain rate ha~~d~~s negligible effect on the ~~homogenized~~ alloyed and homogenized samples:~~. Here,~~ the yield strength ~~is~~remain~~ian~~ed within the scatter bands ~~of the MMSFs~~. In contrast, th~~The~~e strain rate ha~~d~~s interesting effect in the case of T6 treated samples. At 933 s^{-1} the yield strength dropped ~~,~~ and the level of quasi-static yield strength were reached again at the significantly higher, 2629 s^{-1} strain rate. A possible explanation for this phenomena ~~could~~ can be found in the significantly different fracture mechanisms (see Section 3.2).

The structural stiffness was also investigated, and plotted in Fig. 5. In quasi-static conditions, the alloying of the matrix, and the heat treatment ~~have~~ had the same effect on the structural stiffness as in the case of compressive strength. In contrast, at higher strain rates the structural stiffness became higher. In the case of the homogenized MMSFs, the stiffness values remained in a scatter band and~~,~~ the difference between the two higher strain rates was negligible. Meanwhile, in the case of T6 treatment, the difference between the higher strain rates became significant, and higher stiffness values were measured ~~in the case of~~at the 2629 s^{-1} strain rate. ~~As the main important deformation property, T~~the fracture strains were also measured and are shown in Fig. 6. The fracture strains were significantly (~50%) lower in the case of ~~the~~ higher strain rates, and no significant difference between the two high strain rates were observed. This can be explained based on the different fracture mechanisms which correspond to the different loading conditions. In the quasi-static loading case, the occurrence of fracture depended only on the relative strength of the constituents [29]. In contrast, in the case of dynamic loading, the short time impulse of the striking energy ~~does~~ did not allow any structural rearrangement in the composite, resulting in a different failure mechanism, e. g. brittle ruptures instead of plastic deformation (for further details see Section 3.2.). In the case of collision damping, and energy absorption aiming applications, the energy required to initiate the first cracks in the specimens (/

parts) has to be considered. This fracture energy is in strong connection with the compressive strength and fracture strain (the limit of integration) of a component, and therefore, obeyeds the combined trends of both (see Fig. 7). The ascending and descending trends in the case of compressive strength and fracture strains (respectively) were compensated by each other, and the fracture energies became similar within the scatter bands offor the same MMSFs at every tested strain rate. Fig. 7 shows that the T6 heat-treated sample yielded the highest fracture energy, through their correspondingly higher and more beneficial compressive strengths – fracture strain pair. During the testing process, when the fracture energy was reached, the specimen showed a macroscopic failure as it is detailed in Section 3.2. However, the specimens remained intact and more deformation energy could have been absorbed. ; Tthese corresponding absorbed energies are plotted in Fig. 8. In Fig. 8 the absorbed energies (the areas under the engineering stress – engineering strain curves, determined by numerical integration up to the end of the compression) are not completely comparable in the case of different strain rates, because the ends of the deformation process are not the same. In the quasi-static conditions, the compression was continued up to 50%, and the specimens remained intact. In this case, the effect of matrix material was clearly distinguished. However, t;, the T6 treatment seems to bewas relatively slightly beneficial. , but remained altered in the scatter bands only. At higher strain rates the ending strain values of the compression were determined by the process itself. After the impact, the whole curves were registered and plotted as showed in Fig 1b. In the case of increased loading rates the absorbed energies were significantly higher (at least three times higher) at 2629 s^{-1} compared to the tests at 933 s^{-1}, due to the larger ending strain values caused by the larger impact energy. Due toBecause of the discrepancies in the end limit of the integration process, detailed above, and in order to correctly compare and evaluate the effects of matrix composition and heat treatments, Fig. 9a and Fig. 9b were was constructed. Fig. 9a and Fig. 9b shows the overall absorbed energy calculated at the lowest end strain measured for each high strain rate condition, respectively. The end strains of each high strain rate are listed in Table 34. The lowest end strains were measured in the case of Al99.5-O MMSF. These values (2.45% and 8.12% at 933 s^{-1} and at 2629 s^{-1}, respectively) were applied as the upper integration limits in for the calculation of comparable

12

absorbed energies (including the quasi-static tests). Fig. 9 clearly shows the difference in the

loading rates. Based on the 2.45% end limit (Fig. 9a) the higher strain rates ensured absorbed

energies at least two times higher than that displayed at the quasi-static strain rate. Similar

results were observed in the case of 8.12% based comparison (Fig. 9b), where the smallest

increment was about 150 Jcm^{-3}.

3.2. Failure mechanisms

~~To investigate the failure mechanisms, cross-section of the tested specimens were examined.~~

~~The compressed specimens were cut into two halves along their axis, mounted into a resin, and~~

~~grinded on an automatic grinding and polishing machine with SiC papers and diamond~~

~~suspension, respectively. The main parameters of the process are summarized in Table 4 (for~~

~~further details refer to [52-54]).~~ Regarding <u>failure mechanisms,</u> the different ~~matrices the several~~

MMSFs ~~investigated, they~~ had very similar fracture scheme, only the loading rate had significant

effect on the fracture mechanism. In Fig. 10 the failure steps of an Al99.5-O specimen is ~~shown~~

<u>presented</u> at different strain values. Fig. 10a shows the cross section of the specimen after 2%

plastic deformation, where there were no broken hollow spheres <u>(</u>~~,. T~~ <u>t</u>he specimen was

absolutely intact<u>)</u>, ~~showing~~ <u>proving</u> that the initial <u>plastic</u> deformation <u>was originated</u>~~is~~ from the

plastic deformation of the matrix material. Due to the ~~~~<u>6</u>4~~5~~ vol% of the reinforcement, small

displacements <u>between the hollow spheres</u> were possible by the deformation of the matrix

~~between the hollow spheres~~ (the maximal volume fraction of reinforcement would be 74 vol% in

the case of spheres with ~~the same~~<u>identical</u> outer diameter). Fig. 10b represents the specimen

after 30% plastic deformation. A well-defined band with broken spheres can be observed in the

middle of the specimen. The spheres were broken in this region and ~~some~~ <u>a few of them</u> were

completely collapsed. Some barreling due to the friction between the specimen and the tool's

plates is also observable. After further compression, the whole specimen deformed (Fig. 10c),

<u>and</u> the deformation and the failure were diffuse. Due to the gradual nature of the failure, large

amounts of mechanical energy were absorbed during the whole process (Fig. 8).

In Fig. 11 the homogenized, Al99.5-O based MMSF is presented after testing at 933 s^{-1} loading

rate. Some significant differences can be observed in Fig. 11 after 2.45% plastic deformation

13

(see Table 3̶4) compared to the specimens tested in the quasi-static condition. First, while ~2% deformation caused no cracks in the quasi-static condition, all of the hollow spheres exhibited ruptures in their walls at 933 s^{-1} loading rate. The arrows in Fig. 11 point out some of the most obvious cracks that h̶a̶v̶e̶ had occurred in the ceramic microspheres. Moreover these ruptures a̶r̶e̶ were parallel to the loading direction. This phenomenon refers to some additional radial forces caused by some kind of constrain in the deformation (due to the friction between the loading bars and the specimens). Considering this, and the sudden, but relatively low energy loading rate (compared to the higher loading rate), the hollow spheres remained spherical. In the magnified images (Fig. 11b and 11c) i̶t̶ ̶w̶a̶s̶ ̶o̶b̶s̶e̶r̶v̶e̶d̶ some cracks were observed in the matrix between the hollow spheres (designated by ellipses in Fig. 11b and 11c). These cracks appear to h̶a̶v̶e̶ be initiated from the brittle cracks of the hollow spheres (see right side ellipse in Fig. 11c), presumably due to the enlarged gas pressure inside the hollow spheres as suggested by Rabiei et al., b̶u̶t̶ ̶i̶n̶for the case of steel hollow sphere consisting CMFs [46]. The cracks stopped in the matrix material or reached a neighboring hollow sphere and decayed in the interface between the sphere and the matrix material.

In Fig. 12 the Al99.5-O matrix syntactic foam is shown after the highest strain rate compression (at 2629 s^{-1}) up to 8.12% deformation. Due to the higher impact energy of the compression test, the deformation i̶s̶ was significantly larger. The hollow spheres a̶r̶e̶ were completely broken and either flattened or slipped along some main large, almost linear cracks.̶ ̶,̶ ̶a̶n̶d̶ ̶i̶l̶ In some cases, the specimens were separated into two or three parts along these cracks (Fig. 12a). Most of the hollow spheres were broken into numerous particles that h̶a̶v̶e̶ had been removed from their original cavities during the grinding and polishing sequence, leaving dark pores in Fig. 12a. A̶ Two specific example̶s for the broken hollow spheres a̶r̶eis shown in Fig. 12b and 12c. The cracks between the neighboring hollow spheres were significantly larger and wider due to the larger pressure caused by the sudden and relatively large deformation.

D̶u̶e̶ ̶t̶o̶ ̶t̶h̶e̶ ̶e̶x̶t̶e̶n̶s̶i̶v̶e̶l̶y̶ ̶v̶a̶r̶i̶o̶u̶s̶ ̶m̶a̶t̶r̶i̶x̶ ̶m̶a̶t̶e̶r̶i̶a̶l̶s̶ ̶a̶n̶d̶ ̶h̶o̶l̶l̶o̶w̶ ̶s̶p̶h̶e̶r̶e̶ ̶g̶r̶a̶d̶e̶s̶ ̶i̶t̶ ̶i̶s̶ ̶n̶o̶t̶ ̶a̶n̶ ̶o̶b̶v̶i̶o̶u̶s̶ t̶a̶s̶k̶ ̶t̶o̶ ̶c̶o̶m̶p̶a̶r̶e̶ ̶t̶h̶e̶ ̶r̶e̶s̶u̶l̶t̶s̶ ̶o̶f̶ ̶t̶h̶e̶ ̶p̶r̶e̶s̶e̶n̶t̶ ̶p̶a̶p̶e̶r̶ ̶t̶o̶ ̶t̶h̶e̶ ̶d̶a̶t̶a̶ ̶a̶v̶a̶i̶l̶a̶b̶l̶e̶ ̶i̶n̶ ̶t̶h̶e̶ ̶l̶i̶t̶e̶r̶a̶t̶u̶r̶e̶.̶ ̶H̶o̶w̶e̶v̶e̶r̶,̶ s̶o̶m̶e̶ ̶d̶a̶t̶a̶ ̶i̶s̶ ̶l̶i̶s̶t̶e̶d̶ ̶i̶n̶ ̶T̶a̶b̶l̶e̶ ̶5̶,̶ ̶t̶o̶ ̶–̶ ̶a̶t̶ ̶l̶e̶a̶s̶t̶ ̶–̶ ̶s̶i̶t̶u̶a̶t̶e̶ ̶t̶h̶e̶ ̶p̶r̶e̶s̶e̶n̶t̶ ̶m̶a̶t̶e̶r̶i̶a̶l̶s̶ ̶a̶m̶o̶n̶g̶s̶t̶ ̶t̶h̶e̶ ̶f̶o̶a̶m̶s̶ ̶o̶f̶ o̶t̶h̶e̶r̶ ̶r̶e̶s̶e̶a̶r̶c̶h̶ ̶g̶r̶o̶u̶p̶s̶ ̶i̶n̶ ̶t̶h̶e̶ ̶c̶o̶m̶p̶r̶e̶s̶s̶i̶v̶e̶ ̶s̶t̶r̶e̶n̶g̶t̶h̶ ̶p̶o̶i̶n̶t̶ ̶o̶f̶ ̶v̶i̶e̶w̶.̶Due to the large number of

Formatted: Font: Arial, 10 pt, Not Italic

matrix materials and hollow sphere grades reported in the literature, it is not an obvious task to compare these results against other works. However, some efforts have been made on this field, and a literature data has been listed in Table 5, to situate the investigated materials amongst the MMSFs from other research groups. This comparison has been performed from the compressive strength point of view

4. Conclusions

From the detailed and discussed investigations the following conclusions can be drawn.

- The engineering stress – engineering strain curves for quasi-static and high strain rate conditions are significantly different in the case of the investigated MMSFs, however the curves can be effectively analyzed by the application of the same (and standardized) characteristic properties.

- The strain sensitivity values of the investigated MMSFs are very low and originated from the similar sensitivity of the matrix materials.

- The chemical composition of the matrix material, the applied heat treatment and the loading rate have different, but significant effects on the characteristic compressive properties of the MMSFs. Considering the combined effect of these parameters, the compressive properties of the MMSFs can therefore be varied within relatively wide ranges and can be tailored for individual the requirements of given applications.

- The failure modes in quasi-static and dynamic conditions were also different. In the case of quasi-static loading, a slow and diffuse compression of the specimen was observed. The hollow spheres were broken and flattened, the matrix material deformed plastically and the specimen remained intact. In the case of higher loading rates (933 s^{-1}) the nature of the failure changed, due to the restricting effects of the material during the sudden loading. Here, the hollow spheres ruptured linearly. In the case of the highest loading rates (2629 s^{-1}) the hollow spheres were cracked into many pieces, and the specimens broken into two or three large pieces.

- In the case of higher loading rates, cracks were initiated from the brittle ruptures of the hollow spheres, due to the high gas pressure in the spheres caused by the large plastic

15

deformation. The cracks propagated into the matrix material, or reached the

neighboring hollow spheres and decayed in the interface layer. In the case of a higher

loading rate (2629 s^{-1}), larger and wider cracks were observed compared to the lower,

but still dynamic loading rate of (933 s^{-1}).

References

[1] Castro G, Nutt SR. Synthesis of syntactic steel foam using gravity-fed infiltration. Mater Sci Eng A. 2012;553:89-95.

[2] Castro G, Nutt SR. Synthesis of syntactic steel foam using mechanical pressure infiltration. Mater Sci Eng A. 2012;535:274-80.

[3] Weise J, Lehmhus D, Baumeister J, Kun R, Bayoumi M, Busse M. Production and Properties of 316L Stainless Steel Cellular Materials and Syntactic Foams. Steel Res Int. 2014;85(3):486-497.

[4] Luong DD, Shunmugasamy VC, Gupta N, Lehmhus D, Weise J, Baumeister J. Quasi-static and high strain rates compressive response of iron and Invar matrix syntactic foams. Mater Des. 2015;66:516-31.

[5] Peroni L, Scapin M, Avalle M, Weise J, Lehmhus D. Dynamic mechanical behavior of syntactic iron foams with glass microspheres. Mater Sci Eng A. 2012;552:364-75.

[6] Xia X, Feng J, Ding J, Song K, Chen X, Zhao W, Liao B, Hur B et al. Fabrication and characterization of closed-cell magnesium-based composite foams. Mater Des. 2015;74:36-43.

[7] Mondal DP, Datta Majumder J, Jha N, Badkul A, Das S, Patel A, Gupta G et al. Titanium-cenosphere syntactic foam made through powder metallurgy route. Mater Des. 2012;34:82-9.

[8] Xue X-B, Wang L-Q, Wang M-M, Lü W-J, Zhang D. Manufacturing, compressive behaviour and elastic modulus of Ti matrix syntactic foam fabricated by powder metallurgy. Trans Nonferrous Metals Soc China. 2012;22:188-92.

[9] Xue X-B, Zhao Y. Ti matrix syntactic foam fabricated by powder metallurgy: particle breakage and elastic modulus. JOM. 2011;63(2):43-7.

[10] Hollomet GmbH http://www.hollomet.com/home.html, last accessed: 15th June 2015.

[11] Envirospheres Ltd. http://www.envirospheres.com/products.asp, last accessed: 15th June 2015.

[12] Sphere Services Inc. http://www.sphereservices.com/, last accessed 15th June 2015.

[13] 3M Company http://solutions.3m.com/wps/portal/3M/en_US/3M-Defense-US/Defense/Products/~?N=5444948&rt=c3, last accessed: 15th June 2015.

[14] Deep Springs Technology http://teamdst.com/pdf/HollowShells_MTG119-A%20Web.pdf, last accessed: 15th June 2015.

[15] Ceno Technologies http://cenotechnologies.com/, last accessed: 15th June 2015.

[16] Taherishargh M, Belova IV, Murch GE, Fiedler T. Low-density expanded perlite–aluminium syntactic foam. Mater Sci Eng A. 2014;604:127-34.

[17] Taherishargh M, Belova IV, Murch GE, Fiedler T. On the mechanical properties of heat-treated expanded perlite–aluminium syntactic foam. Mater Des. 2014;63:375-83.

[18] Taherishargh M, Sulong MA, Belova IV, Murch GE, Fiedler T. On the particle size effect in expanded perlite aluminium syntactic foam. Mater Des. 2015;66:294-303.

[19] Taherishargh M, Belova IV, Murch GE, Fiedler T. Pumice/aluminium syntactic foam. Mater Sci Eng A. 2015;635:102-8.

16

[20] Tao XF, Zhao YY. Compressive behavior of Al matrix syntactic foams toughened with Al particles. Scripta Mater. 2009;61(5):461-4.

[21] Orbulov IN, Ginsztler J. Compressive behaviour of metal matrix syntactic foams. Acta Polytech Hungarica. 2012;9(2):43-56.

[22] Rohatgi PK, Kim JK, Gupta N, Alaraj S, Daoud A. Compressive characteristics of A356/fly ash cenosphere composites synthesized by pressure infiltration technique. Composites Part A. 2006;37(3):430-7.

[23] Luong DD, Strbik III OM, Hammond VH, Gupta N, Cho K. Development of high performance lightweight aluminum alloy/SiC hollow sphere syntactic foams and compressive characterization at quasi-static and high strain rates. J Alloys Compounds. 2013;550(0):412-22.

[24] Santa Maria JA, Schultz BF, Ferguson JB, Guptan N, Rohatgi PK. Effect of hollow sphere size and size distribution on the quasi-static and high strain rate compressive properties of Al-A380-Al_2O_3 syntactic foams. J Mater Sci. 2014;49:1267-78.

[25] Daoud A, Abou El-khair MT, Abdel-Aziz M, Rohatgi P. Fabrication, microstructure and compressive behavior of ZC63 Mg–microballoon foam composites. Compos Sci Techn. 2007;67(9):1842-53.

[26] Kiser M, He MY, Zok FW. The mechanical response of ceramic microballoon reinforced aluminum matrix composites under compressive loading. Acta Mater. 1999;47(9):2685-94.

[27] Rohatgi P, Gupta N, Schultz B, Luong D. The synthesis, compressive properties, and applications of metal matrix syntactic foams. JOM. 2011;63(2):36-42.

[28] Testing of metallic materials - Compression test of metallic cellular materials, DIN 50134 standard; October 2008.

[29] Balch DK, O'Dwyer JG, Davis GR, Cady CM, Gray Iii GT, Dunand DC. Plasticity and damage in aluminum syntactic foams deformed under dynamic and quasi-static conditions. Mater Sci and Eng A. 2005;391(1–2):408-17.

[30] Luong DD, Gupta N, Daoud A, Rohatgi PK. High strain rate compressive characterization of aluminum alloy/fly ash cenosphere composites. JOM. 2011;63(2):53-6.

[31] Luong DD, Gupta N, Rohatgi PK. The high strain rate compressive response of Mg-Al alloy/fly Ash cenosphere composites. JOM. 2011;63(2):48-52.

[32] Cox J, Luong DD, Shunmugasamy VC, Gupta N, Strbik III OM, Cho K. Dynamic and Thermal Properties of Aluminum Alloy A356/Silicon Carbide Hollow Particle Syntactic Foams. Metals. 2014;4:530-48.

[33] Anantharaman H, Shunmugasamy VC, Strbik III OM, Gupta N, Cho K. Dynamic properties of silicon carbide hollow particle filled magnesium alloy (AZ91D) matrix syntactic foams. Int J Impact Eng. 2015;82:14-24.

[34] Zou LC, Zhang Q, Pang BJ, Wu GH, Jiang LT, Su H. Dynamic compressive behavior of aluminum matrix syntactic foam and its multilayer structure. Mater Des. 2013;45:555-60.

[35] Dou ZY, Jiang LT, Wu GH, Zhang Q, Xiu ZY, Chen GQ. High strain rate compression of cenosphere-pure aluminum syntactic foams. Scripta Mater. 2007;57(10):945-8.

[36] Goel MD, Peroni M, Solomos G, Mondal DP, Matsagar VA, Gupta AK, Larcher M, Marburg S et al. Dynamic compression behavior of cenosphere aluminum alloy syntactic foam. Mater Des. 2012;42:418-23.

[37] Goel MD, Mondal DP, Yadav MS, Gupta SK. Effect of strain rate and relative density on compressive deformation behavior of aluminum cenosphere syntactic foam. Mater Sci Eng A. 2014;590:406-15.

[38] Dass Goel M, Matsagar VA, Gupta AK, Marburg S. Strain rate sensitivity of closed cell aluminium fly ash foam. Trans Nonferrous Metals Soc China. 2013;23(4):1080-9.

[39] Fiedler T, Taherishargh M, Krstulović-Opara L, Vesenjak M. Dynamic compressive loading of expanded perlite/aluminum syntactic foam. Mater Sci Eng A. 2015;626:296-304.

[40] Mondal DP, Goel MD, Das S. Effect of strain rate and relative density on compressive deformation behaviour of closed cell aluminum–fly ash composite foam. Mater Des. 2009;30(4):1268-74.

[41] Mondal DP, Goel MD, Das S. Compressive deformation and energy absorption characteristics of closed cell aluminum-fly ash particle composite foam. Mater Sci and Eng A. 2009;507:102-9.

[42] Peroni L, Scapin M, Avalle M, Weise J, Lehmhus D. Dynamic mechanical behavior of syntactic iron foams with glass microspheres. Mater Sci Eng A. 2012;552:364-75.

[43] Lehmhus D, Weise J, Baumeister J, Peroni L, Scapin M, Fichera C, Avalle M, Busse M et al. Quasi-static and Dynamic Mechanical Performance of Glass Microsphere- and Cenosphere-based 316L Syntactic Foams. Procedia Mater Sci. 2014;4(0):383-7.

[44] Peroni L, Scapin M, Fichera C, Lehmhus D, Weise J, Baumeister J, Avalle M et al. Investigation of the mechanical behaviour of AISI 316L stainless steel syntactic foams at different strain-rates. Composites Part B. 2014;66:430-42.

[45] Rabiei A, Garcia-Avila M. Effect of various parameters on properties of composite steel foams under variety of loading rates. Mater Sci Eng A. 2013;564:539-47.

[46] Alvandi-Tabrizi Y, Whisler DA, Kim H, Rabiei A. High strain rate behavior of composite metal foams. Mater Sci Eng A. 2015;631:248-57.

[47] Alvandi-Tabrizi Y, Rabiei A. Use of Composite Metal Foam for Improving Absorption of Collision Forces. Procedia Mater Sci. 2014;4(0):377-82.

[48] Jaeger HM, Nagel SR. Physics of the Granular State. Science. 1992;5051:1523-31.

[49] Torquato S, Truskett TM, Debenedetti PG. Is Random Close Packing of Spheres Well Defined? Phys Rev Lett. 2000;84(10):2064-7.

[50] Orbulov IN, Dobránszky J. Producing metal matrix syntactic foams by pressure infiltration. Period Polytech Mech Eng. 2008;52(1):35-42.

[51] Orbulov IN, Ginsztler J. Compressive characteristics of metal matrix syntactic foams. Composites Part A. 2012;43(4):553-61.

[52] Orbulov I, Májlinger K. On the microstructure of ceramic hollow microspheres. Period Polytech Mech Eng. 2010;54(2):89-94.

[53] Orbulov IN, Májlinger K. Microstructure of metal-matrix composites reinforced by ceramic microballoons. Mater Techn. 2012;46(4):375-82.

[54] Orbulov IN, Májlinger K. Microstructural aspects of ceramic hollow microspheres reinforced metal matrix composites. Int J Mater Res. 2013;104(9):903-11.

[55] San Marchi C, Cao F, Kouzeli M, Mortensen A. Quasistatic and dynamic compression of aluminum-oxide particle reinforced aluminum. Mater Sci Eng A 2002;337:202-11.

Figure captions

Fig. 1. Typical engineering stress- engineering strain curves of Al99.5-O MMSF for (a) quasi-static and (b) high strain rate loading

Fig. 2. Compressive strength of the investigated MMSFs

Fig. 3. Strain rate sensitivity of the investigated MMSFs

Fig. 4. Yield strength of the investigated MMSFs

Fig. 5. Structural stiffness of the investigated MMSFs

Fig. 6. Fracture strains of the investigated MMSFs

Fig. 7. Fracture energies of the investigated MMSFs

Fig. 8. Absorbed energy values of the investigated MMSFs, measured up to the end of tests

Fig. 9. The absorbed energies of the investigated MMSFs measured up to (a) 2.45% and (b) 8.12% end strains

Fig. 10. Cross-sections of a quasi-statically loaded (0.01 s^{-1}) Al99.5-O specimen at different strains: (a) 2%, (b) 30% and (c) 60%

18

Fig. 11. Cross-sections of an Al99.5-O specimen loaded at 933 s^{-1}, (a) cross section of the full specimen, (b) and (c) magnified parts of the cross section (the loading was vertical)

Fig. 12. Cross-sections of an Al99.5-O specimen loaded at 2629 s^{-1}, (a) cross section of the full specimen, (b) and (c) magnified parts of the cross section (the loading was vertical)

Table captions

Table 1. Properties of the matrix materials

Table 2. Density and porosity values of the produced MMSF blocks Strain rate sensitivity parameters

Table 3. Strain rate sensitivity parameters Average end strain of the investigated MMSFs

Table 4. Average end strain of the investigated MMSFs The parameters of the grinding / polishing process

Table 5. Literature data for the compressive strength and energy absorption capability of similar foams

19

(a)

(b)

Figure3

Figure4
Click here to download high resolution image

Figure5
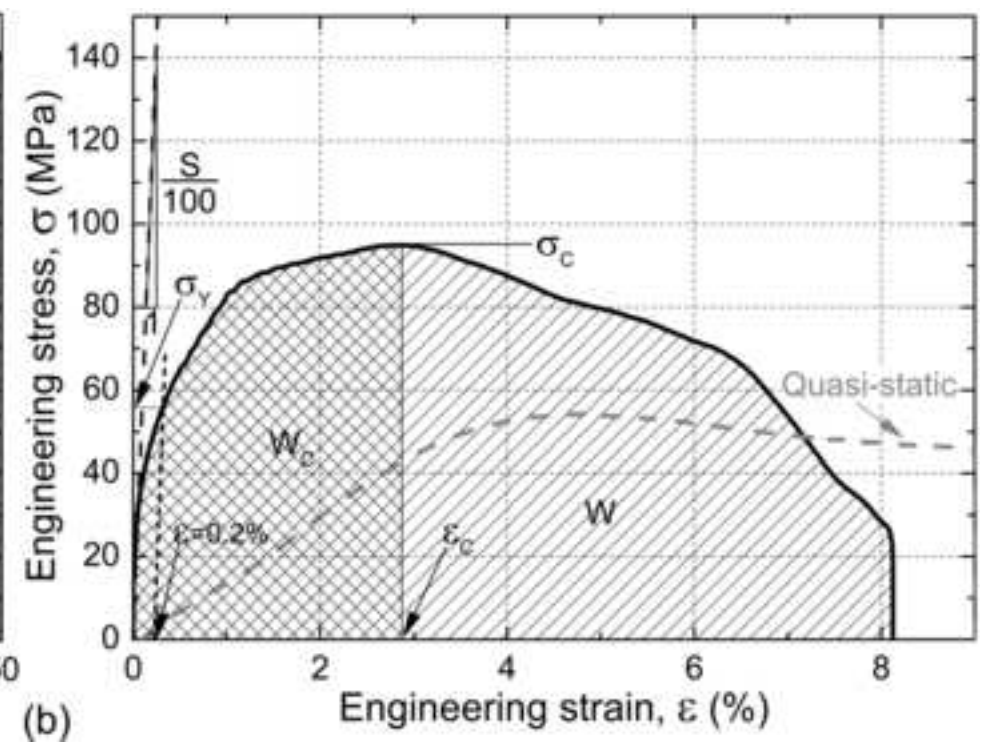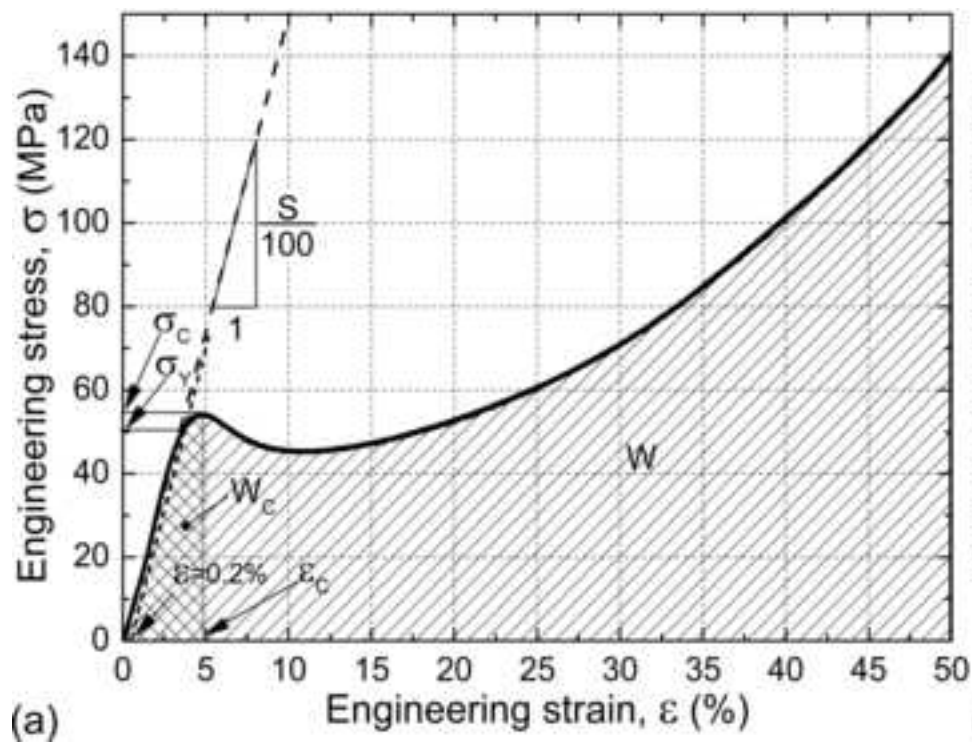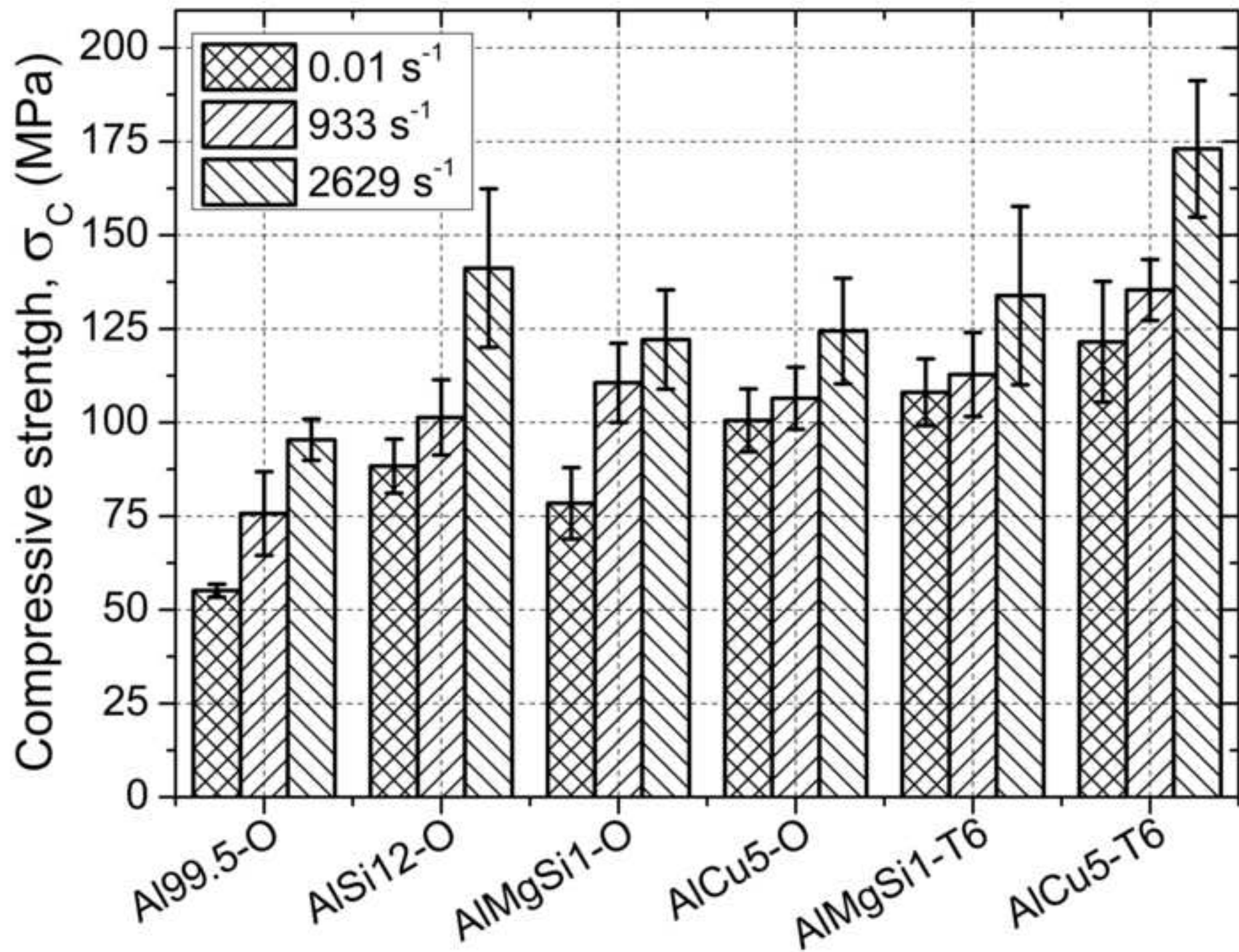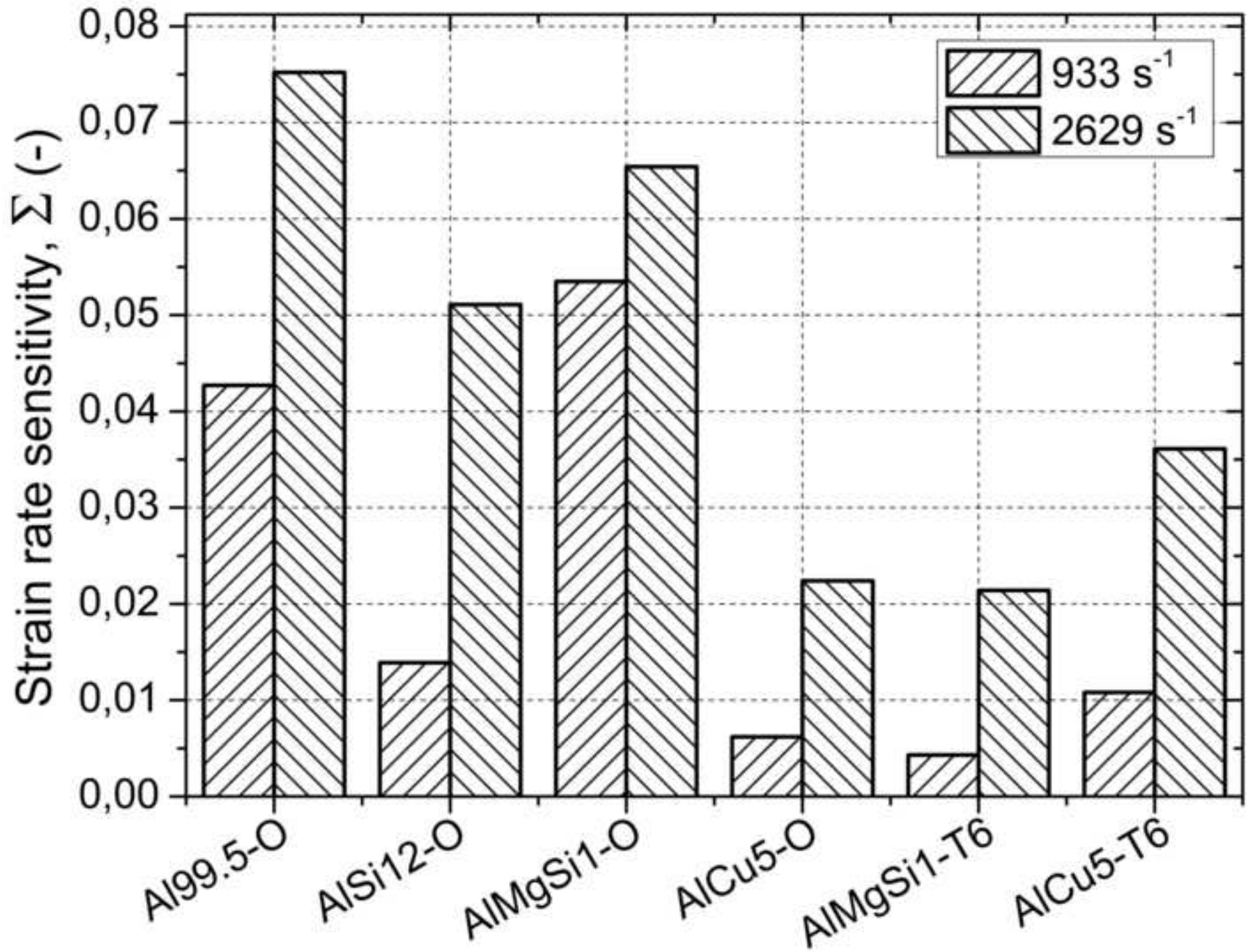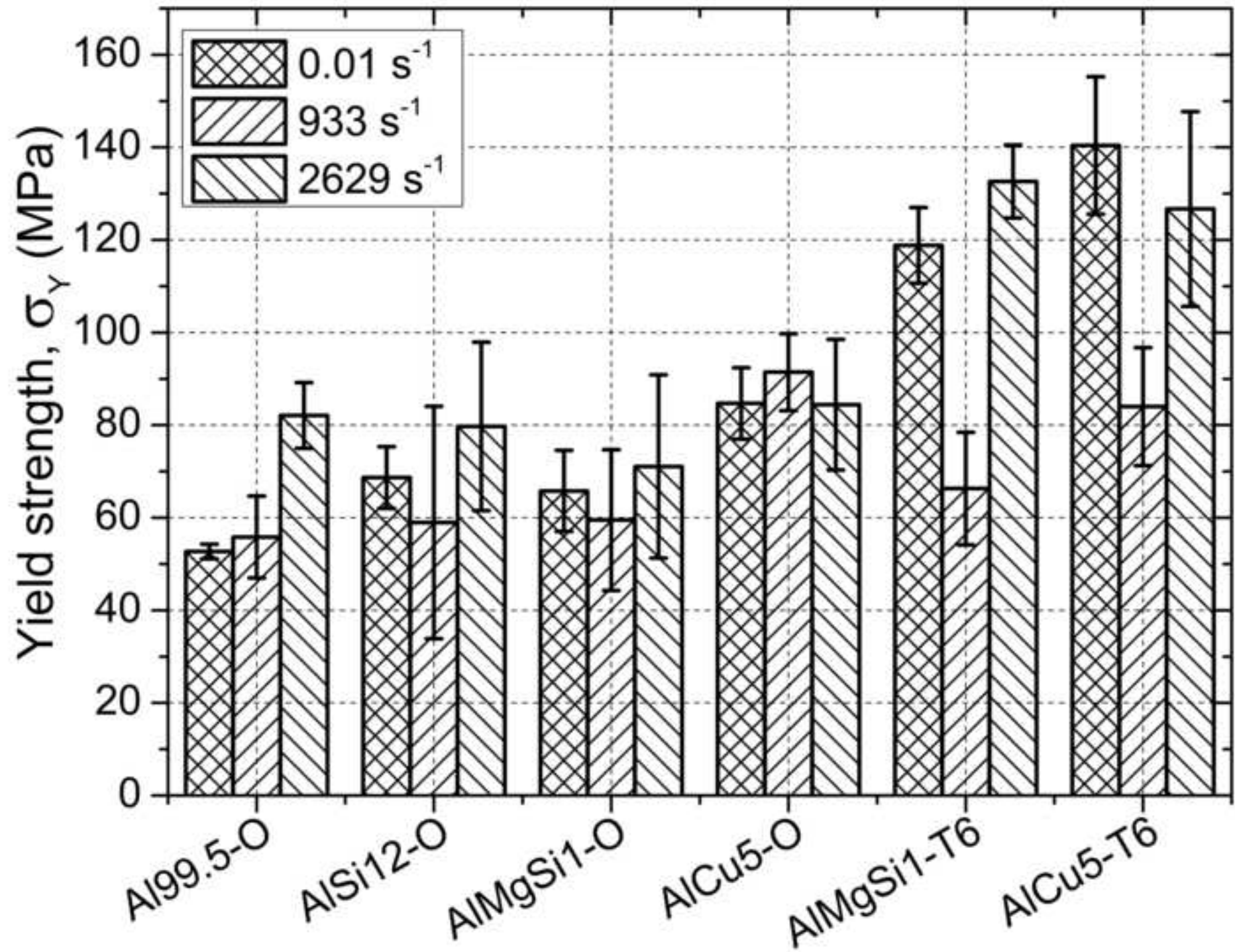**Click here to download high resolution image**

Figure6

Figure7
Click here to download high resolution image

Figure8
Click here to download high resolution image
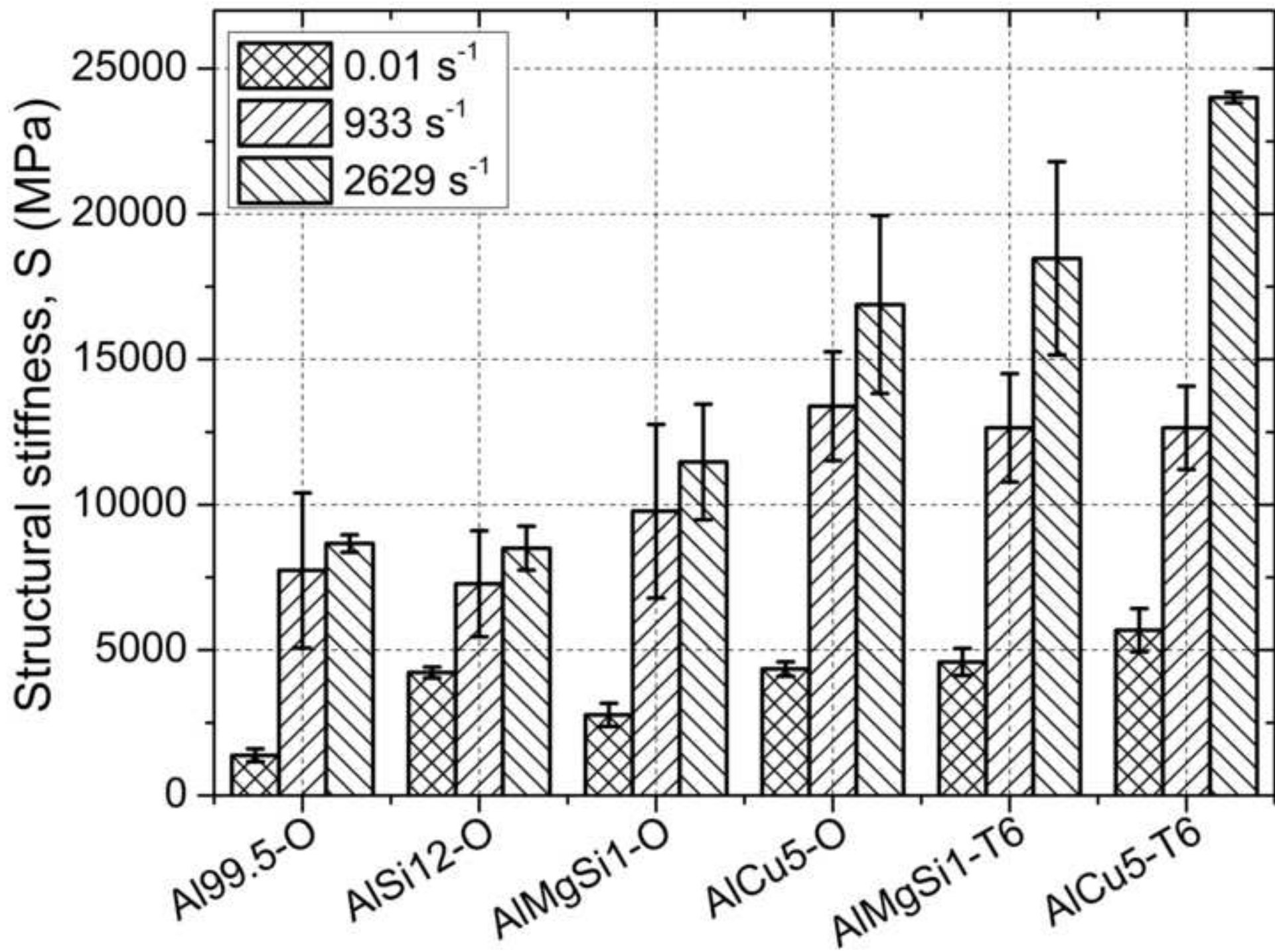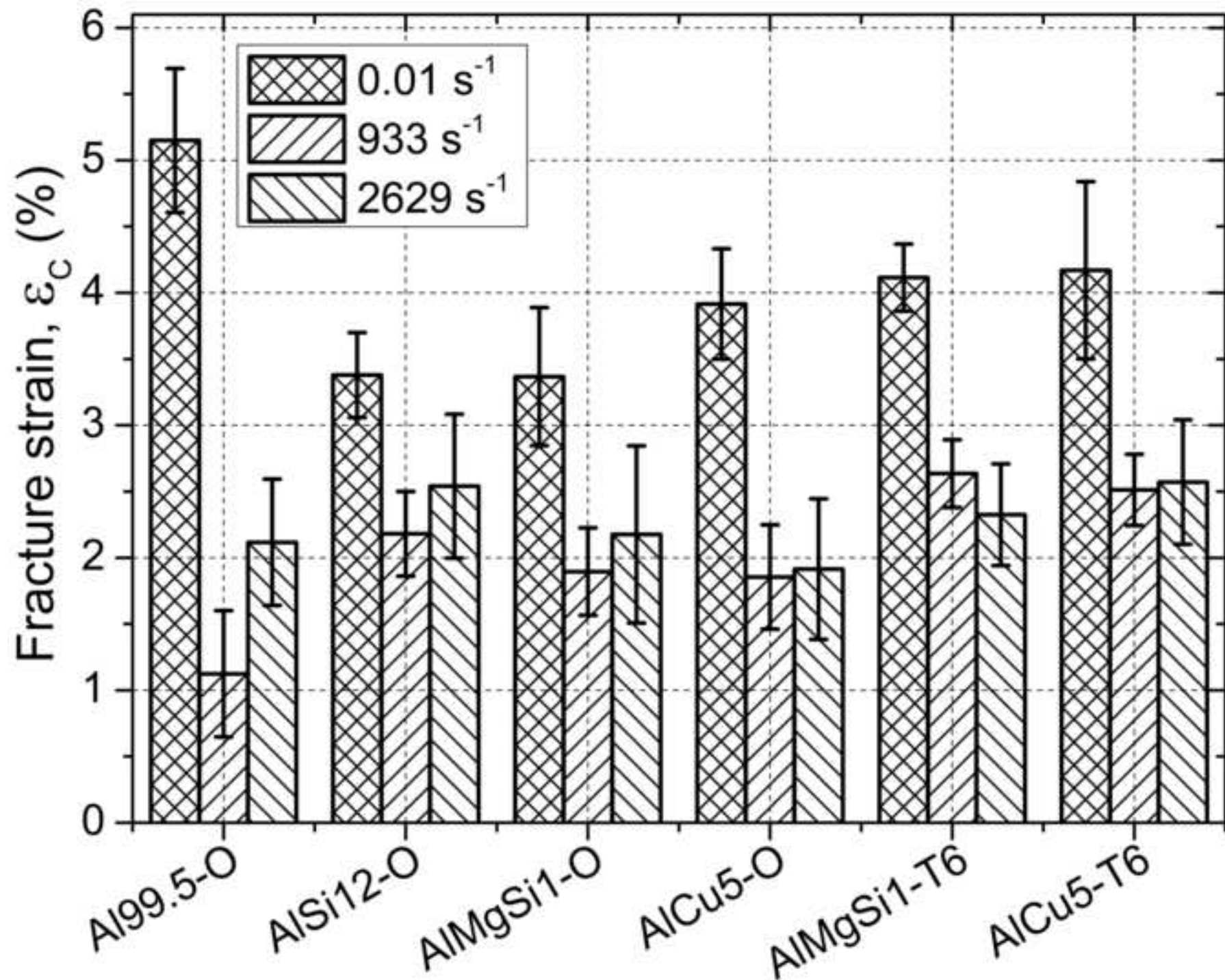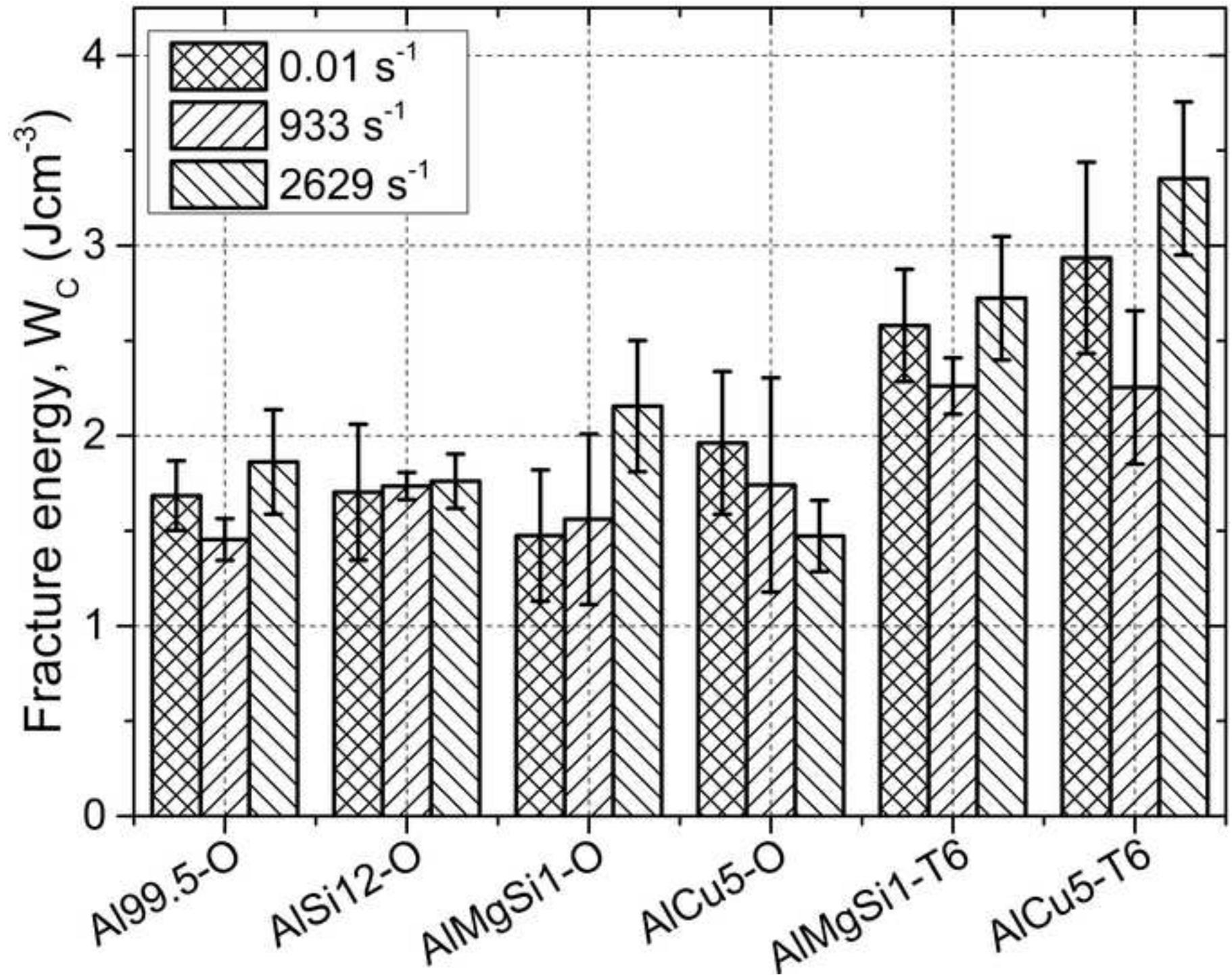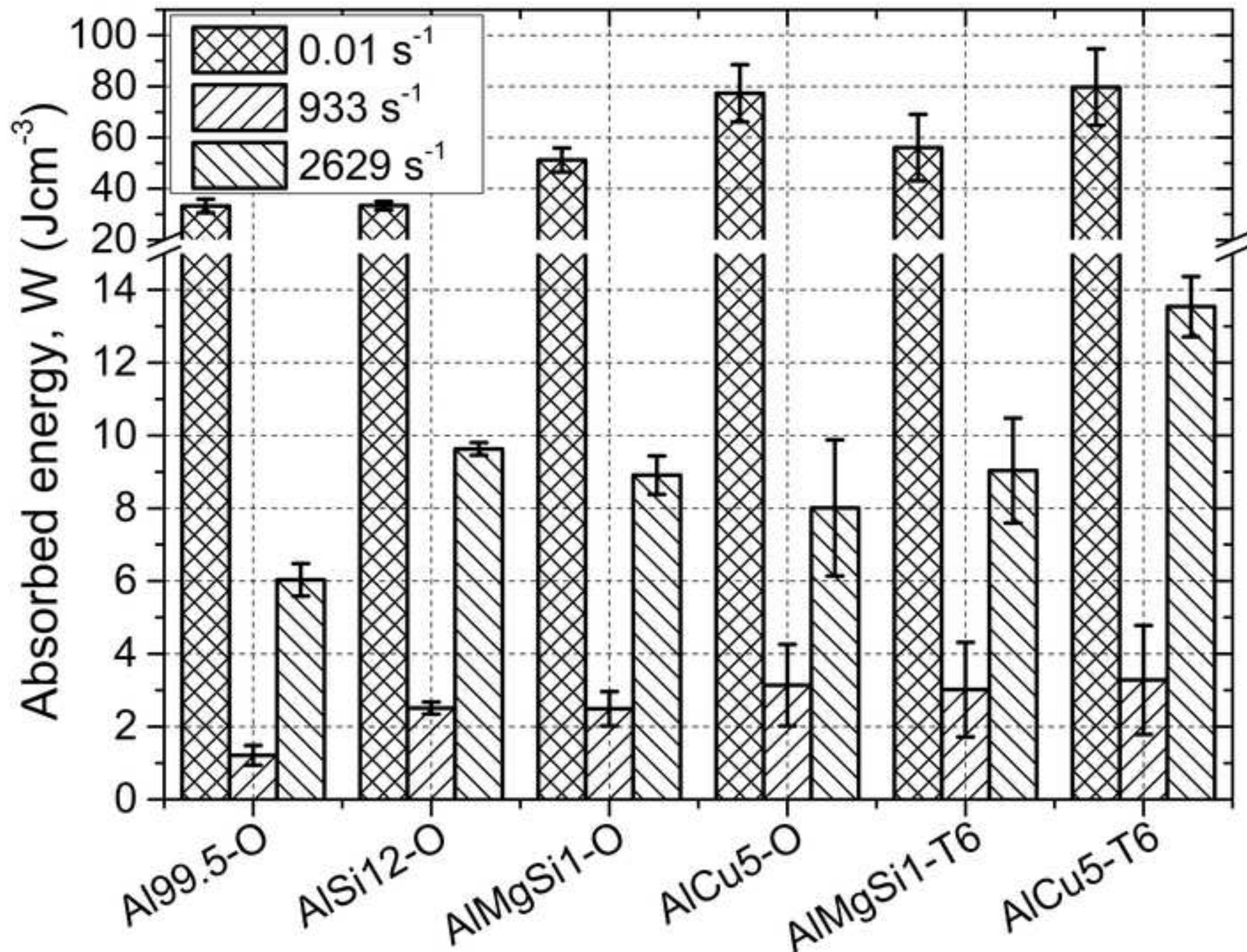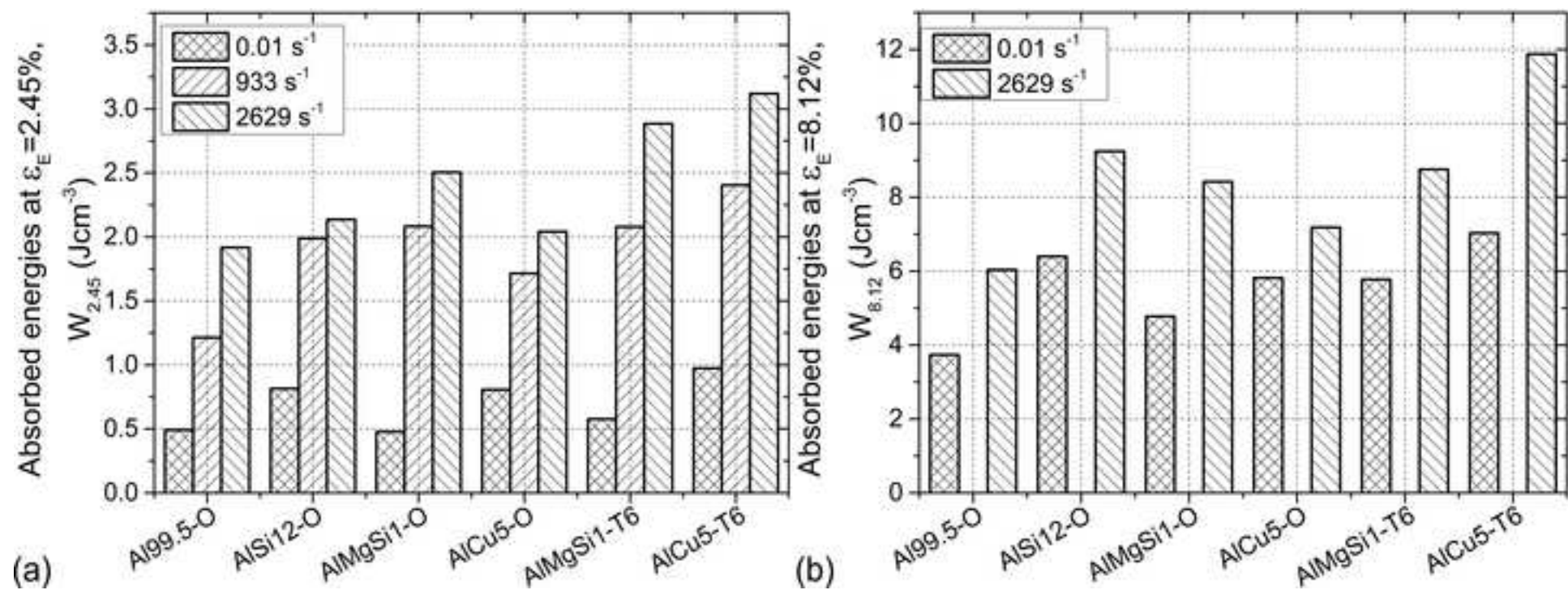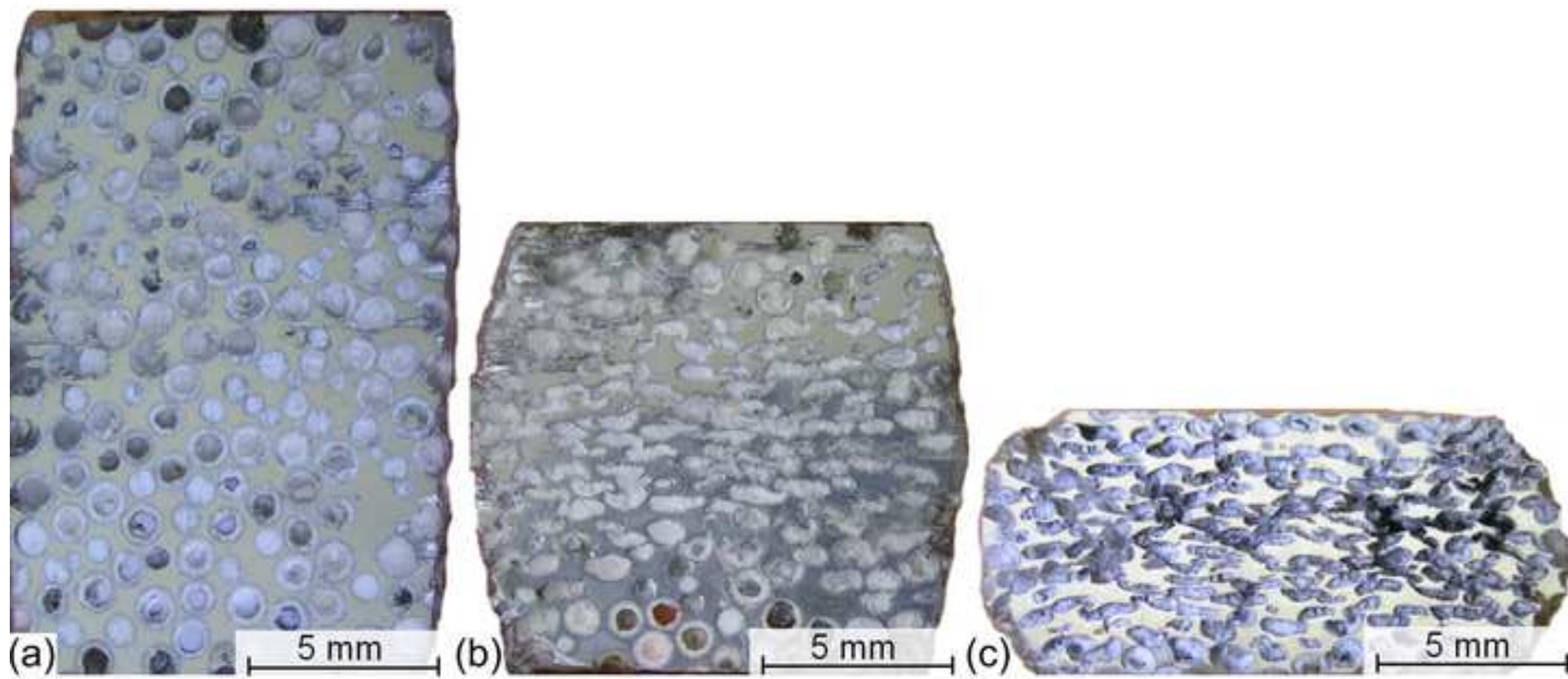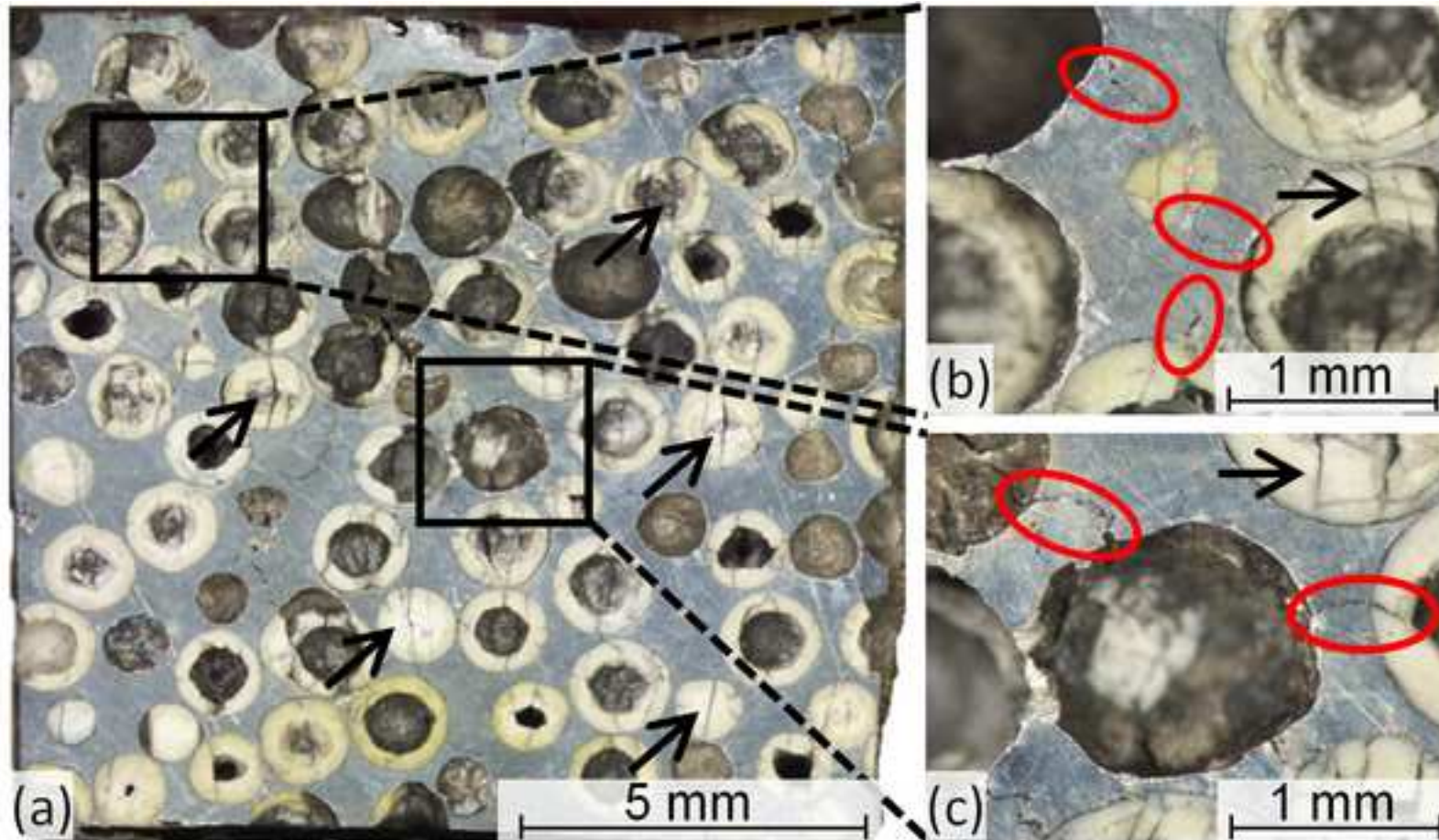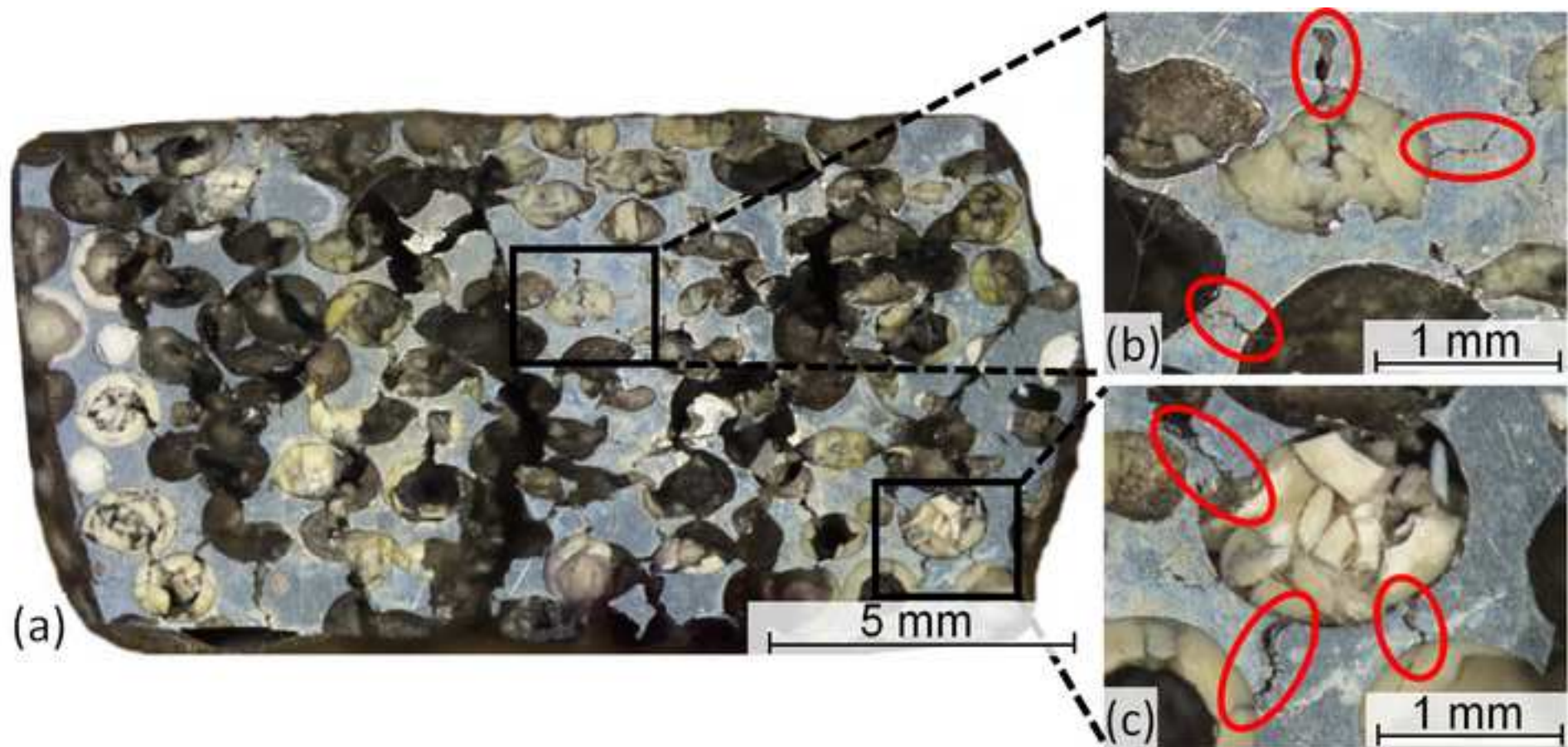
Figure9
Click here to download high resolution image

Figure10
Click here to download high resolution image

(a)　5 mm　(b)　5 mm　(c)　5 mm

Figure12
Click here to download high resolution image

Table(s)

Table 1. Properties of the matrix materials

Matrix	ASM equivalent	Main component (wt%)						UTS (MPa)	$T_{melting}$ °C
		Al	Si	Fe	Mg	Cu	Other		
Al99.5	Al1050	99.5	0.1	0.1	-	-	0.3	75	660
AlSi12	A413.0	86	12.8	0.1	0.1	-	1.0	115	575
AlMgSi1	Al6082*	97	1.1	0.5	1.1	-	0.3	125	650
AlCu5	Al2011	95	-	-	-	4.5	0.5	190	630

*Closest equivalent, significant difference in Mn content that should be 0.4…1 wt%.

Table 2.Density and porosity values of the produced MMSF blocks

Matrix	ρ_M (gcm^{-3})	ρ_S (gcm^{-3})	ρ_T (gcm^{-3})	ρ_R (gcm^{-3})	P_S (%)	P_U (%)	P_T (%)
Al99.5	2.71		1.50	1.83		-7.92	41.86
AlSi12	2.65	0.816	1.48	1.78	49.78	-7.30	42.48
AlMgSi1	2.70		1.49	1.80		-7.49	42.29
AlCu5	2.81		1.53	1.84		-7.29	42.49

Table 3. Strain rate sensitivity parameters

$\dot{\varepsilon}_d$ (s^{-1})	Material	σ_{Cd} (MPa)	σ_{Cq} (MPa)	σ^*(MPa)	Σ
933	Al99.5-O	75.7	55.1	52.7	0.0427
	AlSi12-O	101.3	88.4	101.7	0.0139
	AlMgSi1-O	110.6	78.4	65.8	0.0535
	AlCu5-O	106.4	100.5	104.7	0.0062
	AlMgSi1-T6	112.8	108.1	118.8	0.0043
	AlCu5-T6	135.4	121.5	140.4	0.0108
2629	Al99.5-O	95.4	55.1	52.7	0.0752
	AlSi12-O	141.2	88.4	101.7	0.0511
	AlMgSi1-O	122.1	78.4	65.8	0.0654
	AlCu5-O	124.4	100.5	104.7	0.0224
	AlMgSi1-T6	133.9	108.1	118.8	0.0214
	AlCu5-T6	173.0	121.5	140.4	0.0361

Table 4. Average end strain of the investigated MMSFs

	End strain at 0.01 s^{-1}, $\varepsilon_{E@0.01}$ (%)	End strain at 933 s^{-1}, $\varepsilon_{E@933}$ (%)	End strain at 2629 s^{-1}, $\varepsilon_{E@2629}$ (%)
Al99.5-O	Defined by the test, $\varepsilon_{E@0.01}$=50%	2.45	8.12
AlSi12-O		2.85	8.13
AlMgSi1-O		3.01	8.86
AlCu5-O		3.16	8.72
AlMgSi1-T6		3.03	9.03
AlCu5-T6		3.53	9.43

Table 5. Literature data for the compressive strength and energy absorption capability of similar foams

Matrix	Filler	Compressive strength (MPa)		Energy absorption (Jcm^{-3})		Ref.
		Q-S	Dynamic	Q-S	Dynamic	
Cp-Al	SL75 65 vol% (<75 µm)	109	140@2300 s^{-1}	55@60%	-	[29]
Al7075-O		199	231@2300 s^{-1}	-	-	
Al7075-T6		229	248@2300 s^{-1}	36@25%	-	
Al4032	Fly-ash 5 vol% (44-106 µm)	254	219@754 s^{-1} 256@1293 s^{-1} 280@1629 s^{-1} 288@2136 s^{-1}		- - - -	[30]
A356	SiC$_{HS}$60 vol% (1 mm)	163	124@940 s^{-1} 119@970 s^{-1} 125@1160 s^{-1} 123@1165 s^{-1} 121@1220 s^{-1} 119@1310 s^{-1} 130@1425 s^{-1} 125@1520 s^{-1}		- - - - - - - -	[23] [32]
A380	Al$_2$O$_3$ 40-50 vol% (0-0.5 mm)	165	160@1000 s^{-1}	48@40%	-	[24]
	Al$_2$O$_3$ 40-50 vol% (1-2 mm)	120	140@1000 s^{-1}	39@47%	-	
Al6061	Cenospheres 45 vol% (200 µm)	45	48@2650 s^{-1} 55@3350 s^{-1}	18@47%	28@43@2650 s^{-1} 33@43@3350 s^{-1}	[34]
Cp-Al	Cenospheres 70 vol% (90 µm)	75	108@1400 s^{-1} 114@3000 s^{-1} 119@5000 s^{-1}	27@40%	- - 40@40%@5000 s^{-1}	[35]
	Cenospheres 65 vol% (150 µm)	45	65@2200 s^{-1} 69@4400 s^{-1} 69@5000 s^{-1}	17@40%	- - 29@40%@5000 s^{-1}	
Al2014	Cenospheres 34 vol% (90 µm)	184	190@1 s^{-1} 195@10 s^{-1} 197@420 s^{-1} 223@750 s^{-1} 210@900 s^{-1} 204@1400 s^{-1}	56@30%	56@30%@1 s^{-1} 50@30%@10 s^{-1} - 70@30%@750 s^{-1} 64@30%@900 s^{-1} 60@30%@1400 s^{-1}	[36] [37]
	Cenospheres 35 vol% (200 µm)	161	167@1 s^{-1} 187@10 s^{-1} 206@750 s^{-1} 197@1400 s^{-1}	51@30%	51@30%@1 s^{-1} 50@30%@10 s^{-1} 63@30%@750 s^{-1} 58@30%@1400 s^{-1}	
A356	Globomet 316~65 vol% (2.2 mm)	82	88@1780 s^{-1} 87@1465 s^{-1}	41@50%	43@50%@1780 s^{-1} 43@50%@1465 s^{-1}	[45] [46] [47]
	Globomet 316 ~65 vol% (4 mm)	75	105@1431 s^{-1}	37@50%	38@50%@1431 s^{-1}	
	Globomet 316~65 vol% (5.2 mm)	83	90@1922 s^{-1} 85@767 s^{-1}	5@10%	10@10%@1922 s^{-1} 7@10%@767 s^{-1}	